CRYSTAL GROWTH & DESIGN

Article

Cite This: Cryst. Growth Des. 2017, 17, 5945-5952

pubs.acs.org/crystal

# Precise Facet Engineering of Perovskite Single Crystals by Ligand-Mediated Strategy

Meng-Huan Jao, Chun-Fu Lu, Pao-Yi Tai, and Wei-Fang Su*

Department of Materials Science and Engineering, National Taiwan University, Taipei, Taiwan

Supporting Information

**ABSTRACT:** Inorganic−organic hybrid perovskite single crystals are potential materials for the application of high performance optoelectronic devices. The exposed surface of single crystals can dramatically affect the measured properties. Facet-dependent behaviors are also speculated. However, impeded by the lack of facile facet engineering strategy for inorganic−organic hybrid perovskites, the relationship between different facets and respective performance remains elusive. In this work, we present a simple approach of ligand-mediated crystal growth to control the shape and the exposed facets of methylammonium lead iodide single crystals. The addition of oleylamine ligand can trigger the continuous morphological transition from dodecahedral-shaped single crystal enclosed by $(100)_T$ and $(112)_T$ to cubic-shaped single crystal enclosed by $(110)_T$ and $(002)_T$ while maintaining the material composition and crystalline phase. We fabricated single crystal based photodetectors and carried out the first unambiguous study on the relationship between facet structure and device performance. This report opens a new paradigm to reveal the facet-dependent properties and to enhance the device performance of single crystal.


## INTRODUCTION

Inorganic−organic hybrid perovskite based devices and their rapid progress have recently attracted worldwide attention. They exhibit high optical density, long carrier diffusion length, low trap density, and, above all, high quality polycrystalline thin film that can be easily fabricated through low temperature, solution-processable, and high-throughput deposition methods.[1−4] All these advantages meet the requirement to harvest unlimited renewable energy by cost-efficient and high-performance photovoltaics. Therefore, the inorganic−organic hybrid perovskites have generated tremendous interest in the photovoltaic field. From 2008 until now, the power conversion efficiency of inorganic−organic hybrid perovskite based solar cells have amazingly grown from 3.8% to 22.1%.[5−7] Today the highest recorded efficiency is comparable to the performance of fully developed Si or CdTe based solar cells.[8−13] Inspired by their success in photovoltaics, researchers now find them to be promising candidates as well for photodetectors, light emitting diodes, lasers, spintronics, etc.[14−20]

Despite the phenomenal advance of inorganic−organic hybrid perovskite based optoelectronic devices, one should bear in mind that most of the optoelectronic devices are based on polycrystalline thin films, which are still susceptible to influences caused by defect and abundant grain boundaries.[21,22] Single crystals represent the best solution to address this issue. Possible defects or grain boundary effects can be alleviated. Among the best evidence is the measured carrier diffusion lengths for inorganic−organic hybrid perovskites. In the form of polycrystalline thin film, methylammonium lead iodide ($MAPbI_3$) usually exhibits carrier diffusion length around hundreds of nanometers. On the contrary, diffusion length more than micrometers can be obtained by single crystal samples, which can be attributed to the suppressed carrier recombination rate.[21] Increased diffusion length in single crystals has been realized and utilized to fabricate planar type photodetectors[23,24] and lateral structure photovoltaics.[25] Nevertheless, the structures of the surface are an important parameter to affect the optoelectronic properties of single crystals. For example, given the shallow light penetration depth in inorganic−organic hybrid perovskites, the behavior and application of inorganic−organic hybrid perovskite single crystals are inevitably convoluting from both surface and bulk properties. Therefore, studies focusing on the surface properties of inorganic−organic hybrid perovskite single crystals have increased recently.[26−28]

Several approaches have been reported to make high quality inorganic−organic hybrid perovskite single crystals. Depending on how nucleation is formed, these methods can be classified into three strategies, namely, solution temperature-lowering method,[29,30] inverse temperature crystallization,[31−33] and antisolvent vapor crystallization.[34] Each strategy has its own features and advantages. However, few reports proposed the ability to control exposed facets. For example, in most studies, $MAPbI_3$ single crystals exhibited the exposed facets of $(100)_T$ and $(112)_T$ (the subscripted T indicates the plane index is assigned basis on tetragonal phase).[35,36] To date, only one

Received: July 26, 2017
Revised: September 19, 2017
Published: September 27, 2017





DOI: 10.1021/acs.cgd.7b01040
Cryst. Growth Des. 2017, 17, 5945−5952

study provided a method to selectively expose different facets. Mi et al. demonstrated that the shape of single crystals could be converted between dodecahedral shape and cubic shape by changing the ratio of methylammonium iodide (MAI) to lead iodide ($PbI_2$) in precursor solution.[37] The XRD analysis showed that the cubic-shaped $MAPbI_3$ single crystals were enclosed by $(110)_T$ and $(002)_T$, differing from $(100)_T$ and $(112)_T$ as the ending facets for dodecahedral-shaped ones. The surfaces of single crystals play critical roles with respect to both material properties and device performance. Some studies speculated that the device performance of inorganic−organic hybrid perovskite might be different from the orientations or exposed facets of single crystal.[38,39] Having facet-dependent properties is a common phenomenon in perovskite oxides, especially when they are used as catalysts; their effectiveness depends on surface structures.[40,41] Therefore, the ability to specifically control the exposed facet and the percentage of different exposed facets is essential to grow prefect crystals for outstanding device performance.

Ligand-mediated nanocrystal synthesis is an effective approach to manipulate the shape or size of nanocrystals. The length of ligands, the functional groups of ligands, and the amount of ligands can tune the morphology of nanocrystals. This strategy also works on the synthesis of perovskite nanocrystals. Through the selection of different ligands, inorganic−organic hybrid perovskite nanocrystals can be obtained with different shapes including nanoplates, nanodots, nanorods, and nanoribbons.[42−44]

Inspired by the role of organic ligands in the chemistry of nanocrystal synthesis, we developed a novel ligand-mediated crystal growth method to prepare $MAPbI_3$ single crystals. The precise facet tailoring ability for $MAPbI_3$ single crystals is realized by the mediation of oleylamine. By adding oleylamine in the solution during the growth of single crystals, the frequently observed dodecahedral-shaped single crystals no longer existed. Instead, the cubic-shaped single crystals start to grow. By examining the exposed facets of single crystals by X-ray diffraction, they are cubic-shaped crystals with $(110)_T$ and $(002)_T$ as exposed facets. This kind of single crystal was only reported once in the literature.[37] Moreover, our ligand-mediated strategy provides the ability to fine-tune the exposed ratio between dodecahedral-shaped $(100)_T$ and $(112)_T$ exposed facets and cubic-shaped $(110)_T$ and $(002)_T$. With this, the unambiguous study on the facet-dependent material properties and device performance can be carried out. As a proof of concept, we fabricated the planar type single crystal photodetector based on two representative facets. The devices fabricated on the different facets indeed showed different characteristics of current by varying the voltage. The results highlight the necessity to understand the facet-dependent properties and point out new directions to further improve the performance of device.

## RESULTS AND DISCUSSION

Inverse temperature crystallization was employed to grow the $MAPbI_3$ single crystal. Figure 1 shows both dodecahedral and cubic single crystals can be grown using different solution conditions. In general, dodecahedral-shaped crystal with $(100)_T$ and $(112)_T$ as exposed facets is obtained when the crystal is grown from the solution by mixing only MAI and $PbI_2$ in gamma-butyrolactone (pristine crystal growth solution) and then raising the temperature to 120 °C. Interestingly, in our case, when 0.45 M oleylamine was added into the growth

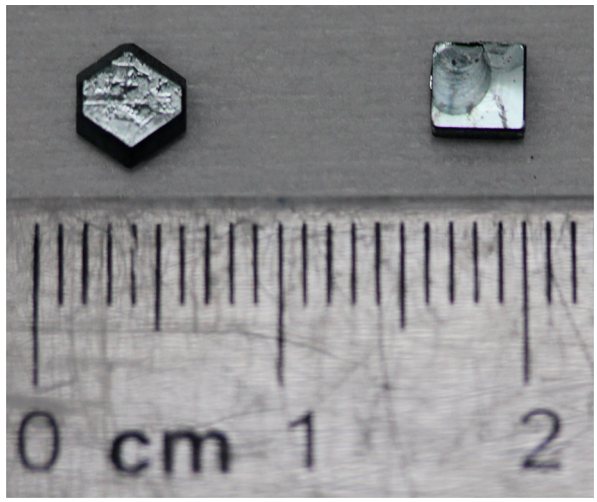


**Figure 1.** Photograph of $MAPbI_3$ single crystals obtained from 0 M (left) and 0.45 M (right) oleylamine.

solution while other parameters remained the same, cubic-shaped single crystal can be obtained. To the best of our knowledge, we are the first to report the success of ligand-mediated single crystal growth technique to control the shape of inorganic−organic hybrid perovskite single crystals in macroscopic scale.

Because all of the angles between each facet in cubic-shaped crystal are 90°, the combination of those exposed facets are no longer $(100)_T$ and $(112)_T$ from dodecahedral crystal. In order to identify the plane index of those exposed facets during the crystal growth, we carefully examined the evolution of exposed facets by varying the growth solution condition. We grew a cubic-shaped crystal in oleylamine-containing solution first. Then we placed the as-prepared crystal into the growth solution without oleylamine. If the shape of the crystal is transformed from cubic to dodecahedral, by comparing the orientation of each exposed facets, the plane indexes of the unknown exposed facets can be deduced.

Figure 2 shows a series of photographs recording the shape evolution of single crystal from cubic to dodecahedral. After placing the cubic-shaped crystal in the pristine growth solution, all of the original exposed facets of cubic crystal started to shrink and finally disappeared. Instead, the features of dodecahedral started to show and eventually the single crystal was enclosed by $(100)_T$ and $(112)_T$. If we consider the four facing-upward diamond-shaped facets to be $(112)_T$ (as framed by blue line in Figure 2), then the four facets facing sideway and perpendicular to each other should be $(100)_T$ (as framed by red line in Figure 2). Because there is a ∼45° rotation between the surface framed by orange line and the $(100)_T$ surfaces, this facet is speculated to be $(110)_T$. The facet facing upward and perpendicular to all $(110)_T$ facets in cubic-shaped crystal should be identified as $(002)_T$ (as framed by green line in Figure 2). This speculation agrees with the simultaneous enlargement of the $(112)_T$ planes during the crystal growth. Thus, we not only successfully index two sets of exposed planes of cubic-shaped $MAPbI_3$ single crystal, but also confirm the function of oleylamine, which can significantly influence the exposed facets.

Bakr et al. demonstrated that the cubic crystal of $EA_xMA_{1-x}PbI_3$ can be obtained by partial replacement of organic cation methylammonium (MA) with ethylammonium (EA) in $MAPbI_3$.[45] The partial replacement of organic cation


DOI: 10.1021/acs.cgd.7b01040
Cryst. Growth Des. 2017, 17, 5945−5952

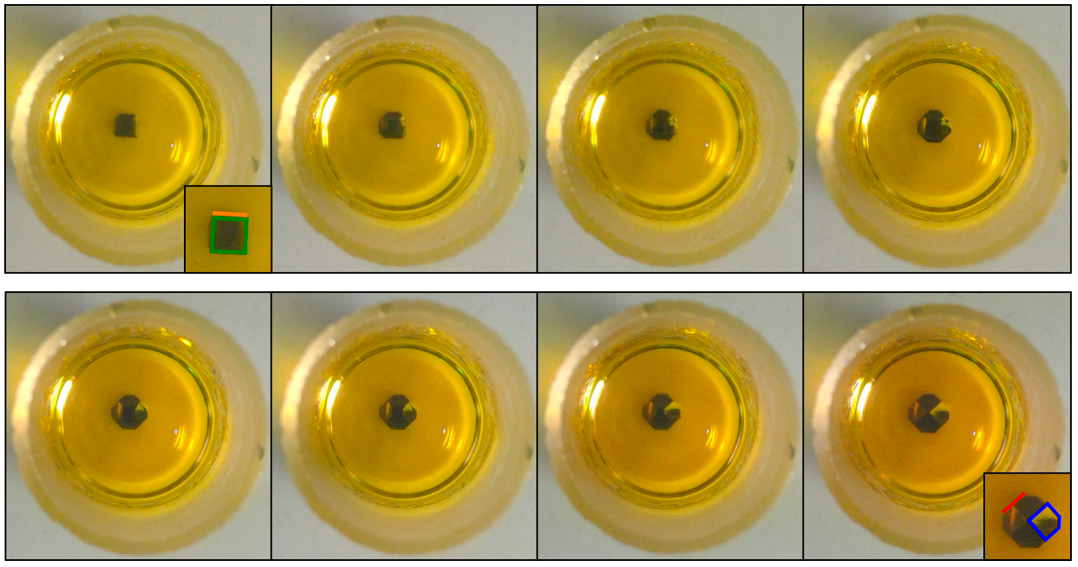

**Figure 2.** Shape evolution of $MAPbI_3$ single crystal. The cubic-shaped crystal was first grown from precursor solution containing 0.45 M oleylamine. Then the crystal was transferred into another precursor solution containing 0 M oleylamine. Several photographs were taken to record the shape evolution.

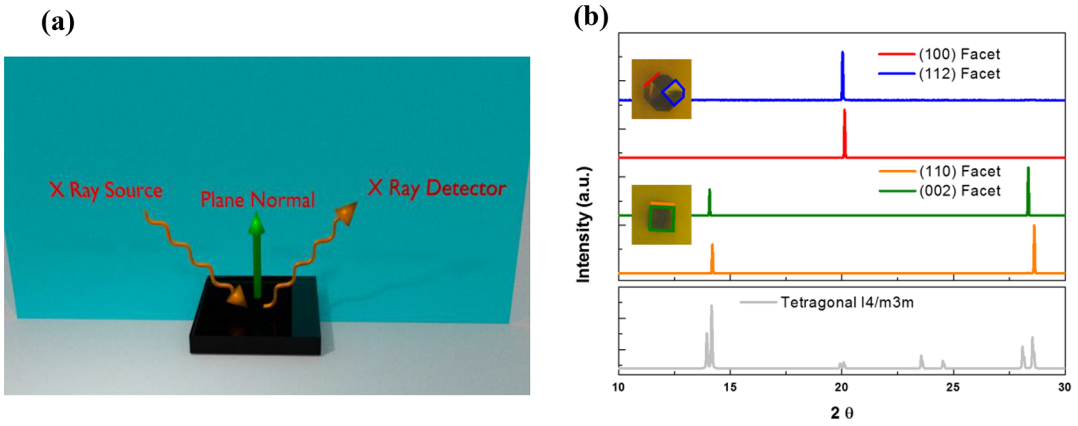


**Figure 3.** (a) Experimental setup for single crystal XRD Analysis. (b) XRD Analysis of $CH_3NH_3PbI_3$ single crystal. Different exposed facets were probed and plane indexes were determined. The inset photographs show the corresponding facets.

leads to alternation of crystallographic symmetry, and the crystal phase is transformed from tetragonal to cubic. In addition, the exposed facets are $(100)_C$ for $EA_xMA_{1-x}PbI_3$ and therefore result in the transformation of crystal shape. Cubic-shaped $EA_xMA_{1-x}PbI_3$ single crystals were obtained rather than dodecahedral-shaped ones. Thus, we wanted to determine the growth mechanism of our crystal transformation. Does it include inserting ligand into the crystal (composition change) or simply changing the exposed facets using ligand as mediated surface control?

We used single crystal X-ray diffraction (XRD) to identify the phase of our cubic-shaped single crystal and also to verify our deduction of newly exposed facets. For comparison, the exposed facets of dodecahedral-shaped single crystal, $(100)_T$ and $(112)_T$, were also examined. The single crystals were placed on a sample holder in a way that the plane normal of exposed facets under examination was parallel to the plane containing both light source and detector, as indicated in Figure 3(a). The results are shown in Figure 3(b). Our data were collected using synchrotron light source with wavelength equal to 1.02 Å. For clarity, the data were then converted as if probed by Cu $K_{\alpha 1}$. For each XRD pattern of $(100)_T$ and $(112)_T$, only single peak at 20.12° and 20.03° are observed, respectively, with clean background, indicating high quality of our dodecahedral-shaped single crystal. The angles of diffraction for $(100)_T$ and $(112)_T$ are very close to each other. It is an evidence that both planes belong to $(110)_C$ in cubic phase and split due to the symmetry breaking when the crystalline phase changes from cubic phase to tetragonal phase (see Figure S1 for atom arrangements of those discussed facets). For the XRD patterns of exposed facets in cubic-shaped single crystals, the diffraction peaks locate at around 14°. This could result from tetragonal $(110)_T$, tetragonal $(002)_T$, or cubic $(100)_C$. To take a closer look at this set of peaks, these peaks are located at different angles (14.19° and 14.07°) instead of showing up at the same position. Therefore, the exposed facets for cubic-shaped crystals are tetragonal phase $(110)_T$ and $(002)_T$. The split is more clear for $(220)_T$ and $(004)_T$ (located at 28.61° and 28.35°, respectively). The powder XRD characterization was also carried out and confirmed the crystalline phase as tetragonal (Figure S2). There is no noticeable shift of peaks or any unassigned peaks, indicating no evidence of incorporation of



DOI: 10.1021/acs.cgd.7b01040
Cryst. Growth Des. 2017, 17, 5945−5952

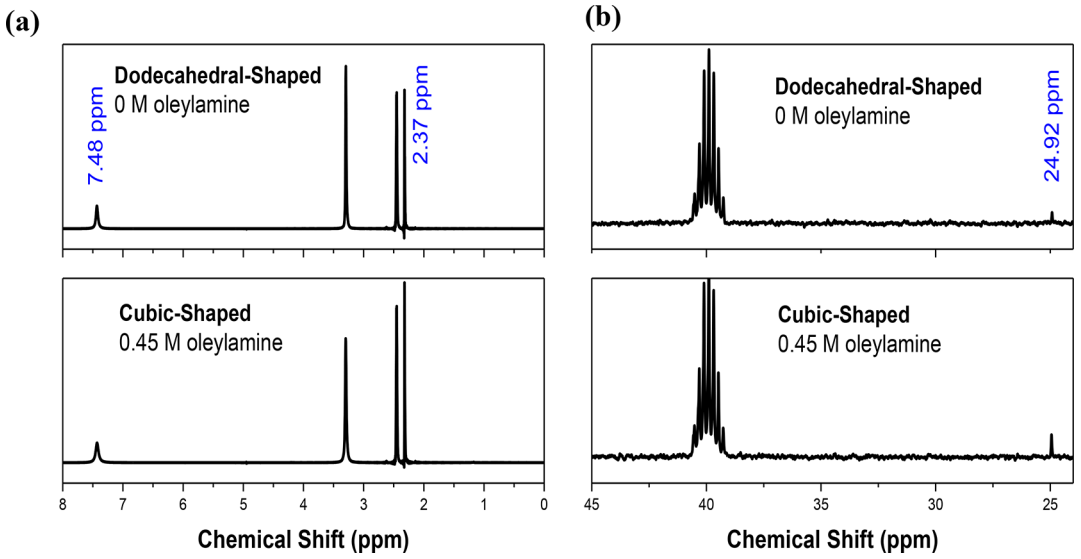


**Figure 4.** (a) $^{1}H$ and (b) $^{13}C$ NMR analysis of dodecahedral- and cubic-shaped single crystals. Deuterated dimethyl sulfoxide was used as solvent to dissolve crystals.

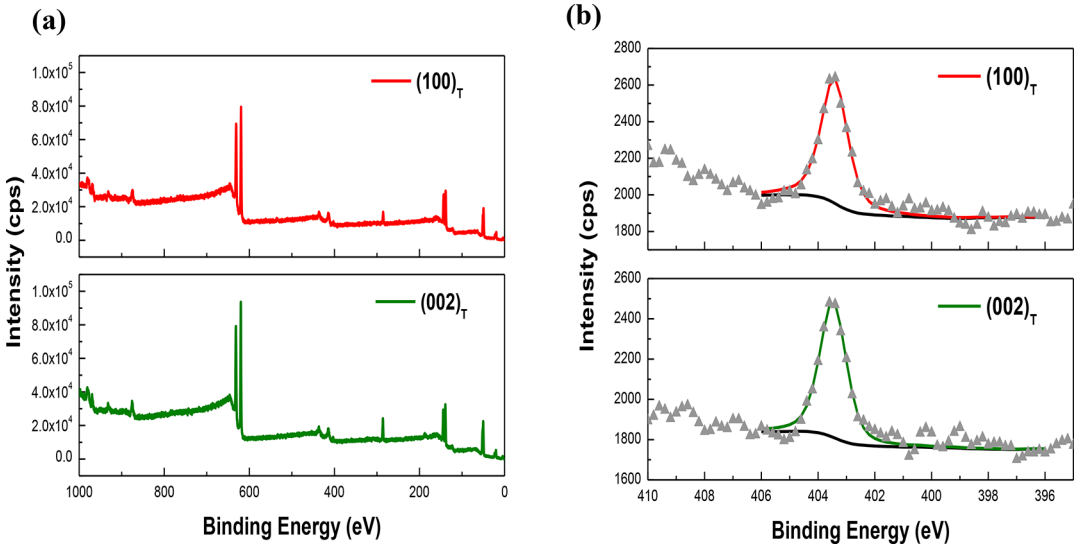


**Figure 5.** X-ray photoelectron spectroscopic analyses of $(100)_T$ and $(002)_T$ facets from dodecahedral- and cubic-shaped single crystals, respectively, (a) survey and (b) high resolution N 1s core level region.

oleylamine into $MAPbI_3$ bulk. This novel ligand-mediated single crystal growth strategy for $MAPbI_3$ can expose two kinds of planes while maintaining the crystal phase and material composition.

To further examine the absence of oleylamine in our cubic-shaped $MAPbI_3$ single crystals, we dissolved the as-growth single crystals in deuterated dimethyl sulfoxide and acquired their solution-phase $^{1}H$ and $^{13}C$ NMR spectra. The results are illustrated in Figure 4. For $^{1}H$ NMR analysis, both dodecahedral- and cubic-shaped single crystals show identical NMR patterns, with the singlet at 2.37 ppm resulting from hydrogen on methyl group and 7.48 ppm resulting from hydrogen on ammonium group. Similarly, both samples show identical patterns from $^{13}C$ NMR analysis. The singlet peak appearing at 24.94 ppm stands for methyl group of methylammonium. A series of peaks near 40 ppm are signals from deuterated dimethyl sulfoxide. No other signal is observed from both spectra, which eliminates the possibility of compositional difference between single crystals harvested from different growing conditions. The results of NMR analysis, combined with the results of powder XRD analysis, prove that oleylamine does not insert or dope into $MAPbI_3$ during the crystal growth process. Accordingly, the oleylamine functions as a ligand that mediates the crystal surface in the growth process of perovskite single crystal. This function is similar to that of colloidal nanocrystal synthesis. The surface chemistry of single crystals was further studied by X-ray photoelectron spectroscopy (XPS). Figure 5 represents the XPS spectra of $(100)_T$ and $(002)_T$ facets for dodecahedral- and cubic-shaped single crystals. Signals from C, N, Pb, and I are detected from both samples. High resolution N 1s core level spectra were recorded. The chemical states of nitrogen affect the binding energy. Binding energy around 403 eV is usually observed for nitrogen from ammonium group, while nitrogen from amine group results in binding energy around 400 eV. For the $(100)_T$ facet, one characteristic peak located at 403.4 eV is



DOI: 10.1021/acs.cgd.7b01040
Cryst. Growth Des. 2017, 17, 5945−5952

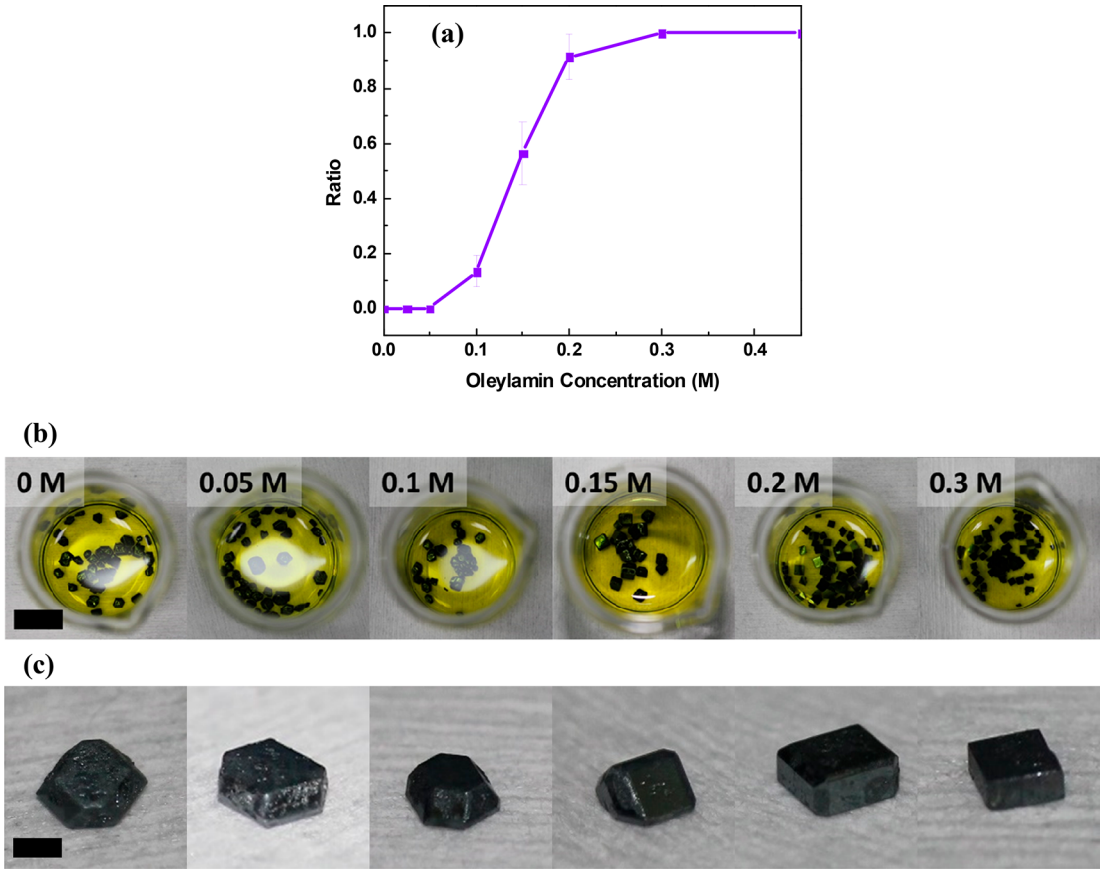


**Figure 6.** $MAPbI_3$ single crystals grown from increased concentration of oleylamine. (a) The exposed facet ratio was calculated according to the concentration of oleylamine. Photographs of crystals (b) in growth solution (scale bar: 10 mm) and (c) representative shape of crystals grown from various oleyelamine concentrations (scale bar: 1.5 mm).

observed, which is contributed from the ammonium group in our single crystal. It is interesting to note that the N 1s core level spectrum of $(002)_T$ facet shows only one peak at 403.4 eV as well, suggesting the absence of other chemical states for nitrogen. The absence of amine group on the $(002)_T$ facet could be explained by the dynamic binding of oleylamine. In our experiments, after the single crystals were harvested from the growth solution, the residual solvent on the surface of single crystals was cleaned by Kimwipes. This procedure was to avoid any damage on the surface. We speculate that physically adsorbed oleylamine was detached easily during wiping. Therefore, no signal corresponding to oleylamine is observed from the $(002)_T$ facet by the surface characterization of XPS.

The ability of oleylamine to control the exposed facets and thus the crystal shape was further verified by varying the concentration of oleylamine. The precursor solutions of $MAPbI_3$ with the concentration of oleylamine ranging from 0 to 0.45 M were prepared. Single crystals were grown and harvested from those solutions. In these experiments we deliberately added a small amount of unfiltered growth solution to serve as nucleation sites so that large amount of small-sized crystals would grow from the same batch of solution. Then we did statistics by calculating the facets exposed ratio. Because oleylamine can facilitate the exposure of $(002)_T$ and $(110)_T$ facets, we defined the ratio $R_{(002)T+(110)T}$

$$R_{(002)_T+(110)_T} = \frac{\text{Surface area of } (002)_T + (110)_T}{\text{Total surface area}}$$

The detailed procedure of calculation is given in Supporting Information. Figure 6 shows the average $R_{(002)T+(110)T}$ as a function of the amount of oleylamine. When the concentration of oleylamine was below 0.05 M, all the single crystals were enclosed by $(100)_T$ and $(112)_T$, so the crystal shape was dodecahedral. Between 0.05 and 0.3 M, the increase of oleylamine concentration would increase the exposed percentages of $(110)_T$ and $(002)_T$ facets, leading to the shape evolution from dodecahedral to truncated cubic. When the oleylamine concentration surpassed 0.3 M, crystals exhibited only $(110)_T$ and $(002)_T$ as exposed facets. The corresponding crystal shape was cubic. This is the first report in the literature by adopting ligand-mediated single crystal growth strategy for inorganic−organic hybrid perovskite and successfully tailoring the ratio of different exposed facets.

We speculate that the mechanism of controlling exposed facets by oleylamine is due to the change of surface energy. The $(110)_T$ and $(002)_T$ surfaces of $MAPbI_3$ possess lower surface energy than $(100)_T$ and $(112)_T$ when coordinated with oleylamine. For instance, when 3D hybrid perovskite is sliced down into 2D layered hybrid perovskite by long chain ammonium cations, those long chain ammonium cations always coordinated on the $(100)_C$ surface,[46] which is crystallographically equal to $(110)_T$ and $(002)_T$. Also, it has been shown recently that the long chain ammonium can bind to the $(100)_C$ surface of $FAPbI_3$ via ionic interaction and further reduces the surface energy.[47] In our case, when oleylamine (or its dynamically protonated counterpart) is incorporated in single crystal growth solution, it is prone to



DOI: 10.1021/acs.cgd.7b01040
Cryst. Growth Des. 2017, 17, 5945−5952

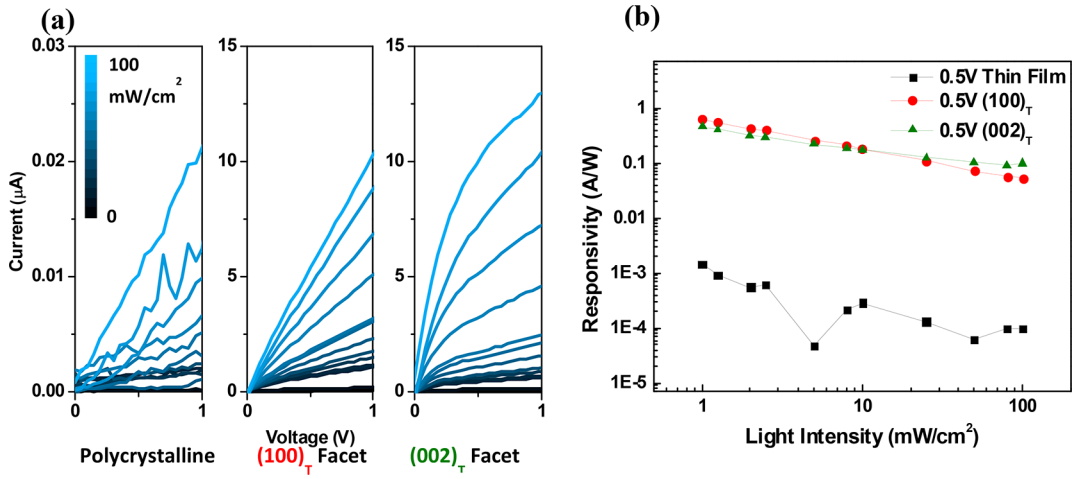


**Figure 7.** Planar type photodetector performance. (a) I–V characterization curves. Note that the scale of current for polycrystalline device is different from those for single crystal devices. (b) Calculated responsivity at 0.5 V of photodetectors based on polycrystalline thin film, single crystal $(100)_T$ facet, and single crystal $(002)_T$ facet.

bind on $(110)_T$ and $(002)_T$ of $MAPbI_3$ and leads to slower growth rates of those facets. As a result, single crystal with $(110)_T$ and $(002)_T$ as ending facets is obtained.

The ligand-mediated single crystal growth strategy can precisely control the ratio of exposed facets for $MAPbI_3$. Additionally, from the results of XPS analysis, the ligand no longer existed once the crystal was harvested from the growth solution. Hence, it provides us an opportunity to acquire more information about the facet-dependent behavior in pristine inorganic–organic hybrid perovskite. Recently, inorganic–organic hybrid perovskite single crystals have been extensively used to fabricate highly responsive photodetectors. Depending on the composition and band gap of the inorganic–organic hybrid perovskite, the response spectra can range from visible light, ultraviolet light, to X-ray.[48−51] The key factors for the successful development of inorganic–organic hybrid perovskite single crystal photodetectors lie in the intrinsic material properties, including high absorption coefficient, remarkably low trap density, long carrier lifetime, and excellent carrier transport abilities. We used our single crystals to examine the facet-dependent behavior by fabricating photodetectors on different facets.

The planar type device structure of photodetectors was chosen because the direction of carrier transport could be limited along the plane of exposed facet as much as possible. The $(100)_T$ and $(112)_T$ are similar in terms of crystallography for tetragonal phase $MAPbI_3$ (as shown in Figure S1), and they are actually identical when $MAPbI_3$ undergoes transform from tetragonal to cubic phase. The same argument can be applied on $(110)_T$ and $(002)_T$. Therefore, we selected two representative facets, $(100)_T$ and $(002)_T$, to test their photoresponse on the fabricated devices. The AM 1.5 G white light with intensity ranging from 1 to 100 $mW/cm^2$ was shed on the single crystal photodetectors; the photocurrents were recorded with varied voltage biases. The results are shown in Figure 7. A polycrystalline thin film photodetector was also fabricated for comparison. Both photodetectors based on single crystal exhibit large photocurrent, and outperform their polycrystalline counterpart by nearly 3 orders of magnitude. The figure-of-merit, responsivity, standing for the ratio of photocurrent versus light bias intensity, is calculated at 0.5 V. The definition of responsivity can be written as

$$R = \frac{I_{ph}}{P_0 \times A}$$

where $I_{ph}$ stands for the difference of currents between light and dark, $P_0$ stands for irradiance light intensity, and $A$ stands for device area. The responsivity for both photodetectors based on single crystals also exhibits higher values than their counterpart polycrystalline one, which can be attributed to longer carrier diffusion length and lower trap density in single crystals. The difference of responsivity between $(100)_T$ and $(002)_T$ based photodetectors is not large. Both devices achieve responsivity of ~0.5 A/W at light intensity of 1 $mW/cm^2$. However, the two exposed facets show quite different characteristics of current–voltage curves under various light bias. At a fixed light bias, the photocurrent on $(002)_T$ facet increases rapidly as the increase of voltage from 0 to ~0.2 V. Above that voltage range, the slope of current to voltage is decreased, and the increase of photocurrent is reduced. On the contrary, the $(100)_T$ based photodetector shows no significant change of slope as the voltage swept from 0 to 15 V. We speculate that this phenomenon may result from ionic migration in inorganic–organic hybrid perovskite. It is reported that when applying voltage on inorganic–organic hybrid perovskite, the iodide anion will drift and gradually result in built-in potential with direction opposite to the externally applied bias. As a consequence, the effective voltage, the applied voltage minus the internal potential, based on inorganic–organic hybrid perovskite becomes smaller. This may explain the decrease of slope in the $(002)_T$ based photodetector. Therefore, this result may indicate that the ionic migration in $(002)_T$ facet is higher than that of $(100)_T$ facet.

In summary, we developed a ligand-mediated crystal growth strategy to manipulate the exposed facets of $MAPbI_3$ single crystals. Well-controlled ratio of exposed facets between $(100)_T$, $(112)_T$ and $(110)_T$, $(002)_T$ in $MAPbI_3$ single crystals can be continuously tailored by adjusting the amount of oleylamine in growth solution. The facet-dependent device performance is unambiguously investigated for the first time, revealing different current–voltage behaviors between different facets in $MAPbI_3$. The simplicity of obtaining high quality single crystals with targeted exposed facets by our ligand-mediated strategy opens a new avenue to gain more insight in


DOI: 10.1021/acs.cgd.7b01040
Cryst. Growth Des. 2017, 17, 5945−5952

the fundamental properties of inorganic−organic hybrid perovskites. Extensive studies on facet-dependent performance for applications in solar cells, photodetectors, field-effect transistors, and photocatalysts are worth pursuing. We hope this work can not only expand the potential applications for inorganic−organic hybrid perovskites but also lead to advances in their performance.

## EXPERIMENTAL SECTION

**Facet-Engineering of $MAPbI_3$ Single Crystals.** Lead iodide (99%), gamma-butyrolactone (99+%), and oleylamine (80−90%) were purchased from ACROS. Methylammonium iodide (>98%) was purchased from FrontMaterials. All chemicals were used as received without any purification. For a typical growth of $MAPbI_3$ single crystals, precursor solution was prepared by dissolving lead iodide (1 mmol) and methylammonium iodide (1 mmol) in gamma-butyrolactone (1 mL) at 70 °C. The millimeter sizes of single crystals were prepared by filtering the growth solution through 0.45 μm PTFE filter to minimize nucleation sites. Various amounts of oleylamine (0−0.45 M) was added into the precursor solution to tailor the shape and ratio of exposed facets. In order to grow cubic-shaped single crystal enclosed with $(110)_T$ and $(002)_T$, oleylamine more than 0.3 M was needed. Glass vial containing precursor solution was placed on hot plate. When the temperature reached around 120 to 140 °C, the crystal started to grow within 30 min and the growth was continued until the desired the size was obtained.

**XRD Characterization.** Single crystal XRD patterns were collected on beamline 13A1, National Synchrotron Radiation Research Center, Taiwan. The wavelength of light source was 1.02 Å. Powder XRD patterns were collected by PANalytical, X'Pert PRO using Cu $K_{\alpha 1}$ as light source and PIXcel1D as detector.

**NMR Analysis.** The as-prepared single crystals were dissolved in *d*-DMSO with concentration of 30 mg/mL for both $^1H$ and $^{13}C$ NMR characterizations. All spectra were recorded on Bruker DPX 400 MHz NMR.

**XPS Measurement.** The X-ray photoelectron spectrometry (XPS) (ULVACPHI, Chigasaki, Japan) was used to examine the core-levels of our single crystals by using Al $K_\alpha$ radiation with a photoelectron take off angle of 45° in high vacuum ($\sim 10^{-6}$ Torr).

**Fabrication and Characterization of Photodetectors.** 100 nm gold was thermally deposited as electrodes through shadow mask on selected facets of single crystals. The gap of electrodes was 100 μm. The measurement of planar type photodetectors was conducted by a probe station in ambient condition, with relative humidity around 40%. Simulated AM1.5G white light was employed as light source. Light intensity was controlled by neutral density filter from 1 to 100 $mW/cm^2$. A source meter (Keithley 2410) was used to record the I−V characterization curves.

## ASSOCIATED CONTENT

### Supporting Information

The Supporting Information is available free of charge on the ACS Publications website at DOI: 10.1021/acs.cgd.7b01040.

Surface structures of different exposed facets, powder XRD data, and calculation method of exposed facets ratio (PDF)

## AUTHOR INFORMATION


### Corresponding Author

*E-mail: suwf@ntu.edu.tw.

### ORCID

Wei-Fang Su: 0000-0002-3375-4664


### Notes

The authors declare no competing financial interest.

## ACKNOWLEDGMENTS

The authors thank the Ministry of Science and Technology of Taiwan for the financial support of this research (106-3113-E-002-008-CC2; 106-2923-M-002-004-MY3, 106-2119-M-002-030). The authors also thank Dr. Shih-Chang Weng (National Synchrotron Radiation Research Center of Taiwan), Shun-Hsiang Chan and Ting-Han Lin (Chang Guan University) for valuable discussions on the characterization and measurement of using single crystal X-ray diffraction spectroscopy.

## REFERENCES


(1) Snaith, H. J. *J. Phys. Chem. Lett.* **2013**, *4*, 3623−3630.
(2) Park, N.-G. *J. Phys. Chem. Lett.* **2013**, *4*, 2423−2429.
(3) Gao, P.; Grätzel, M.; Nazeeruddin, M. K. *Energy Environ. Sci.* **2014**, *7*, 2448−2463.
(4) Chen, Q.; De Marco, N.; Yang, Y.; Song, T.-B.; Chen, C.-C.; Zhao, H.; Hong, Z.; Zhou, H.; Yang, Y. *Nano Today* **2015**, *10*, 355−396.
(5) Kojima, A.; Teshima, K.; Shirai, Y.; Miyasaka, T. *J. Am. Chem. Soc.* **2009**, *131*, 6050−6051.
(6) Yang, W. S.; Noh, J. H.; Jeon, N. J.; Kim, Y. C.; Ryu, S.; Seo, J.; Seok, S. I. *Science* **2015**, *348*, 1234−1237.
(7) Saliba, M.; Matsui, T.; Domanski, K.; Seo, J.-Y.; Ummadisingu, A.; Zakeeruddin, S. M.; Correa-Baena, J.-P.; Tress, W. R.; Abate, A.; Hagfeldt, A.; Grätzel, M. *Science* **2016**, *354*, 206−209.
(8) Chang, C.-Y.; Chu, C.-Y.; Huang, Y.-C.; Huang, C.-W.; Chang, S.-Y.; Chen, C.-A.; Chao, C.-Y.; Su, W.-F. *ACS Appl. Mater. Interfaces* **2015**, *7*, 4955−4961.
(9) Conings, B.; Babayigit, A.; Klug, M. T.; Bai, S.; Gauquelin, N.; Sakai, N.; Wang, J. T.; Verbeeck, J.; Boyen, H. G.; Snaith, H. J. *Adv. Mater.* **2016**, *28*, 10701−10709.
(10) Wang, Q.; Dong, Q.; Li, T.; Gruverman, A.; Huang, J. *Adv. Mater.* **2016**, *28*, 6734−6739.
(11) Saliba, M.; Matsui, T.; Seo, J. Y.; Domanski, K.; Correa-Baena, J. P.; Nazeeruddin, M. K.; Zakeeruddin, S. M.; Tress, W.; Abate, A.; Hagfeldt, A.; Gratzel, M. *Energy Environ. Sci.* **2016**, *9*, 1989−1997.
(12) Ye, F.; Chen, H.; Xie, F.; Tang, W.; Yin, M.; He, J.; Bi, E.; Wang, Y.; Yang, X.; Han, L. *Energy Environ. Sci.* **2016**, *9*, 2295−2301.
(13) Liao, H.-C.; Guo, P.; Hsu, C.-P.; Lin, M.; Wang, B.; Zeng, L.; Huang, W.; Soe, C. M. M.; Su, W.-F.; Bedzyk, M. J.; Wasielewski, M. R.; Facchetti, A.; Chang, R. P. H.; Kanatzidis, M. G.; Marks, T. J. *Adv. Electron. Mater.* **2017**, *7*, 1601660.
(14) Sutherland, B. R.; Johnston, A. K.; Ip, A. H.; Xu, J.; Adinolfi, V.; Kanjanaboos, P.; Sargent, E. H. *ACS Photonics* **2015**, *2*, 1117−1123.
(15) Chiba, T.; Hoshi, K.; Pu, Y.-J.; Takeda, Y.; Hayashi, Y.; Ohisa, S.; Kawata, S.; Kido, J. *ACS Appl. Mater. Interfaces* **2017**, *9*, 18054−18060.
(16) Li, J.; Si, J. J.; Gan, L.; Liu, Y.; Ye, Z. Z.; He, H. P. *ACS Appl. Mater. Interfaces* **2016**, *8*, 32978−32983.
(17) Gao, L.; Zeng, K.; Guo, J.; Ge, C.; Du, J.; Zhao, Y.; Chen, C.; Deng, H.; He, Y.; Song, H.; Niu, G.; Tang, J. *Nano Lett.* **2016**, *16*, 7446−7454.
(18) Zhu, H.; Fu, Y.; Meng, F.; Wu, X.; Gong, Z.; Ding, Q.; Gustafsson, M. V.; Trinh, M. T.; Jin, S.; Zhu, X. Y. *Nat. Mater.* **2015**, *14*, 636−642.
(19) Xiao, Z.; Kerner, R. A.; Zhao, L.; Tran, N. L.; Lee, K. M.; Koh, T.-W.; Scholes, G. D.; Rand, B. P. *Nat. Photonics* **2017**, *11*, 108−115.
(20) Giovanni, D.; Chong, W. K.; Dewi, H. A.; Thirumal, K.; Neogi, I.; Ramesh, R.; Mhaisalkar, S.; Mathews, N.; Sum, T. C. *Sci. Adv.* **2016**, *2*, e1600477.
(21) Huang, J.; Shao, Y.; Dong, Q. *J. Phys. Chem. Lett.* **2015**, *6*, 3218−3227.
(22) Yang, D.; Ming, W.; Shi, H.; Zhang, L.; Du, M.-H. *Chem. Mater.* **2016**, *28*, 4349−4357.
(23) Saidaminov, M. I.; Adinolfi, V.; Comin, R.; Abdelhady, A. L.; Peng, W.; Dursun, I.; Yuan, M.; Hoogland, S.; Sargent, E. H.; Bakr, O. M. *Nat. Commun.* **2015**, *6*, 8724.




DOI: 10.1021/acs.cgd.7b01040
*Cryst. Growth Des.* 2017, 17, 5945−5952

(24) Lian, Z.; Yan, Q.; Lv, Q.; Wang, Y.; Liu, L.; Zhang, L.; Pan, S.; Li, Q.; Wang, L.; Sun, J. L. *Sci. Rep.* **2015**, *5*, 16563.
(25) Dong, Q.; Song, J.; Fang, Y.; Shao, Y.; Ducharme, S.; Huang, J. *Adv. Mater.* **2016**, *28*, 2816−2821.
(26) Murali, B.; Yengel, E.; Yang, C.; Peng, W.; Alarousu, E.; Bakr, O. M.; Mohammed, O. F. *ACS Energy Lett.* **2017**, *2*, 846−856.
(27) Wu, B.; Nguyen, H. T.; Ku, Z.; Han, G.; Giovanni, D.; Mathews, N.; Fan, H. J.; Sum, T. C. *Adv. Energy Mater.* **2016**, *6*, 1600551.
(28) Sarmah, S. P.; Burlakov, V. M.; Yengel, E.; Murali, B.; Alarousu, E.; El-Zohry, A. M.; Yang, C.; Alias, M. S.; Zhumekenov, A. A.; Saidaminov, M. I.; Cho, N.; Wehbe, N.; Mitra, S.; Ajia, I.; Dey, S.; Mansour, A. E.; Abdelsamie, M.; Amassian, A.; Roqan, I. S.; Ooi, B. S.; Goriely, A.; Bakr, O. M.; Mohammed, O. F. *Nano Lett.* **2017**, *17*, 2021−2027.
(29) Dong, Q.; Fang, Y.; Shao, Y.; Mulligan, P.; Qiu, J.; Cao, L.; Huang, J. *Science* **2015**, *347*, 967−970.
(30) Lian, Z.; Yan, Q.; Gao, T.; Ding, J.; Lv, Q.; Ning, C.; Li, Q.; Sun, J. L. *J. Am. Chem. Soc.* **2016**, *138*, 9409−9412.
(31) Liu, Y.; Yang, Z.; Cui, D.; Ren, X.; Sun, J.; Liu, X.; Zhang, J.; Wei, Q.; Fan, H.; Yu, F.; Zhang, X.; Zhao, C.; Liu, S. F. *Adv. Mater.* **2015**, *27*, 5176−5183.
(32) Rakita, Y.; Kedem, N.; Gupta, S.; Sadhanala, A.; Kalchenko, V.; Bohm, M. L.; Kulbak, M.; Friend, R. H.; Cahen, D.; Hodes, G. *Cryst. Growth Des.* **2016**, *16*, 5717−5725.
(33) Saidaminov, M. I.; Abdelhady, A. L.; Murali, B.; Alarousu, E.; Burlakov, V. M.; Peng, W.; Dursun, I.; Wang, L.; He, Y.; Maculan, G.; Goriely, A.; Wu, T.; Mohammed, O. F.; Bakr, O. M. *Nat. Commun.* **2015**, *6*, 7586.
(34) Shi, D.; Adinolfi, V.; Comin, R.; Yuan, M.; Alarousu, E.; Buin, A.; Chen, Y.; Hoogland, S.; Rothenberger, A.; Katsiev, K.; Losovyj, Y.; Zhang, X.; Dowben, P. A.; Mohammed, O. F.; Sargent, E. H.; Bakr, O. M. *Science* **2015**, *347*, 519−522.
(35) Shamsi, J.; Abdelhady, A. L.; Accornero, S.; Arciniegas, M.; Goldoni, L.; Kandada, A. R.; Petrozza, A.; Manna, L. *ACS Energy Lett.* **2016**, *1*, 1042−1048.
(36) Baikie, T.; Fang, Y.; Kadro, J. M.; Schreyer, M.; Wei, F.; Mhaisalkar, S. G.; Graetzel, M.; White, T. J. *J. Mater. Chem. A* **2013**, *1*, 5628−5641.
(37) Zhang, Y.; Huang, F.; Mi, Q. *Chem. Lett.* **2016**, *45*, 1030−1032.
(38) Foley, B. J.; Girard, J.; Sorenson, B. A.; Chen, A. Z.; Scott Niezgoda, J.; Alpert, M. R.; Harper, A. F.; Smilgies, D.-M.; Clancy, P.; Saidi, W. A.; Choi, J. J. *J. Mater. Chem. A* **2017**, *5*, 113−123.
(39) Leblebici, S. Y.; Leppert, L.; Li, Y.; Reyes-Lillo, S. E.; Wickenburg, S.; Wong, E.; Lee, J.; Melli, M.; Ziegler, D.; Angell, D. K.; Ogletree, D. F.; Ashby, P. D.; Toma, F. M.; Neaton, J. B.; Sharp, I. D.; Weber-Bargioni, A. *Nat. Energy* **2016**, *1*, 16093.
(40) Huang, K.; Yuan, L.; Feng, S. *Inorg. Chem. Front.* **2015**, *2*, 965−981.
(41) Bai, S.; Wang, L.; Li, Z.; Xiong, Y. *Adv. Sci.* **2017**, *4*, 1600216.
(42) Pan, A.; He, B.; Fan, X.; Liu, Z.; Urban, J. J.; Alivisatos, A. P.; He, L.; Liu, Y. *ACS Nano* **2016**, *10*, 7943−7954.
(43) Kirakosyan, A.; Kim, J.; Lee, S. W.; Swathi, I.; Yoon, S.-G.; Choi, J. *Cryst. Growth Des.* **2017**, *17*, 794−799.
(44) Shamsi, J.; Dang, Z.; Bianchini, P.; Canale, C.; Di Stasio, F.; Brescia, R.; Prato, M.; Manna, L. *J. Am. Chem. Soc.* **2016**, *138*, 7240−7243.
(45) Peng, W.; Miao, X.; Adinolfi, V.; Alarousu, E.; El Tall, O.; Emwas, A. H.; Zhao, C.; Walters, G.; Liu, J.; Ouellette, O.; Pan, J.; Murali, B.; Sargent, E. H.; Mohammed, O. F.; Bakr, O. M. *Angew. Chem., Int. Ed.* **2016**, *55*, 10686−10690.
(46) Stoumpos, C. C.; Cao, D. H.; Clark, D. J.; Young, J.; Rondinelli, J. M.; Jang, J. I.; Hupp, J. T.; Kanatzidis, M. G. *Chem. Mater.* **2016**, *28*, 2852−2867.
(47) Fu, Y. P.; Wu, T.; Wang, J.; Zhai, J. Y.; Shearer, M. J.; Zhao, Y. Z.; Hamers, R. J.; Kan, E. J.; Deng, K. M.; Zhu, X.-Y.; Jin, S. *Nano Lett.* **2017**, *17*, 4405−4414.
(48) Wei, H.; Fang, Y.; Mulligan, P.; Chuirazzi, W.; Fang, H.-H.; Wang, C.; Ecker, B. R.; Gao, Y.; Loi, M. A.; Cao, L.; Huang, J. *Nat. Photonics* **2016**, *10*, 333−339.
(49) Wei, W.; Zhang, Y.; Xu, Q.; Wei, H.; Fang, Y.; Wang, Q.; Deng, Y.; Li, T.; Gruverman, A.; Cao, L.; Huang, J. *Nat. Photonics* **2017**, *11*, 315−321.
(50) Dirin, D. N.; Cherniukh, I.; Yakunin, S.; Shynkarenko, Y.; Kovalenko, M. V. *Chem. Mater.* **2016**, *28*, 8470−8474.
(51) Zheng, E.; Yuh, B.; Tosado, G. A.; Yu, Q. *J. Mater. Chem. C* **2017**, *5*, 3796−3806.


DOI: 10.1021/acs.cgd.7b01040
*Cryst. Growth Des.* 2017, 17, 5945−5952